

Quasi-Deterministic Channel Model for mmWaves: Mathematical Formalization and Validation

Mattia Lecci*, Michele Polese[‡], Chiehping Lai[†], Jian Wang[†], Camillo Gentile[†], Nada Golmie[†], Michele Zorzi*

*Department of Information Engineering, University of Padova, Italy, e-mail: {name.surname}@dei.unipd.it

[‡]Institute for the Wireless Internet of Things, Northeastern University, Boston, MA, USA, e-mail: m.polese@northeastern.edu

[†]National Institute of Standards and Technology (NIST), Gaithersburg, MD, USA, e-mail: {name.surname}@nist.gov

Abstract—5G and beyond networks will use, for the first time ever, the millimeter wave (mmWave) spectrum for mobile communications. Accurate performance evaluation is fundamental to the design of reliable mmWave networks, with accuracy rooted in the fidelity of the channel models. At mmWaves, the model must account for the spatial characteristics of propagation since networks will employ highly directional antennas to counter the much greater pathloss. In this regard, Quasi-Deterministic (QD) models are highly accurate channel models, which characterize the propagation in terms of clusters of multipath components, given by a reflected ray and multiple diffuse components of any given Computer Aided Design (CAD) scenario. This paper introduces a detailed mathematical formulation for QD models at mmWaves, that can be used as a reference for their implementation and development. Moreover, it compares channel instances obtained with an open source NIST QD model implementation against real measurements at 60 GHz, substantiating the accuracy of the model. Results show that, when comparing the proposed model and deterministic rays alone with a measurement campaign, the Kolmogorov-Smirnov (KS) test of the QD model improves by up to 0.537.

Index Terms—5G, millimeter wave, channel model, 3GPP, IEEE, quasi deterministic

I. INTRODUCTION

To satisfy a constantly growing demand for mobile connectivity, the future generations of wireless networks will exploit frequencies above 6 GHz for radio access. This portion of the spectrum, loosely identified as the millimeter wave (mmWave) band, features large chunks of untapped spectrum, to be used to provide ultra-high data rates to end users. In this regard, cellular networks implementing the 3GPP NR Release 15 specifications can support a carrier frequency of up to 52.6 GHz, while IEEE 802.11ad/ay foresees Wireless Local Area Networks (WLANs) operating in the unlicensed spectrum at 60 GHz. The development of robust mobile networks in this frequency range is challenging. The high propagation loss, indeed, limits the coverage of the mmWave base stations and access points. Besides, mmWave signals are blocked by common obstacles (e.g., the human body, walls, vehicles) with high penetration losses, making the power of the received signal highly variable.

This work was partially supported by NIST under Award No. 70NANB18H273. Mattia Lecci's activities were supported by *Fondazione CaRiPaRo* under the grants "Dottorati di Ricerca" 2018.

A reliable and accurate evaluation of the performance is fundamental to the development of technological solutions for mmWave cellular networks. Given the difficulties associated to a testbed setup at such high frequencies, the research community has, so far, mostly relied on analysis and simulations [1], developing several tools for different protocol stacks and proposed communication technologies [2]–[4]. The accuracy of the performance evaluation, however, depends to a large degree on the fidelity of the representation of the channel [5]. When it comes to mmWaves, the complex dynamics of the propagation environment strengthen the need for a comprehensive model, which accounts not only for the pathloss, but also for the spatial behavior of the signal propagation and its interaction with directional antennas, and for the fading that arises from the interaction with the scatterers in the environment [6].

This need has sparked several research efforts aimed at characterizing the mmWave channel. Measurement campaigns have been conducted in diverse settings, e.g., in urban or rural scenarios [7], [8], or indoors [9], [10]. These works have identified a number of key elements for the modeling of mmWave channels [11], [12]: (i) the multipath components are sparse in the angular domain, and this impacts the characterization and design of beamforming schemes; (ii) blockage affects the link dynamics much more than at sub-6 GHz; (iii) effects of diffuse scattering from rough surfaces become more prominent at shorter wavelengths. So far, different modeling approaches have emerged in the mmWave domain. The simplest ones are used, generally, for mathematical analysis, and characterize fading with Nakagami-m or Rayleigh random variables, often with simplified beamforming patterns [1]. The 3rd Generation Partnership Project (3GPP) has adopted a Spatial Channel Model (SCM) for the evaluation of NR in the frequency range between 0.5 and 100 GHz, in which a channel matrix is generated with a purely stochastic approach [13]. These approaches, however, cannot fully capture the fading and angular components of the mmWave channel that relate with a *realistic* and *specific* propagation environment.

This can be achieved using a Ray-Tracer (RT) [14], which models the channel by generating the Multi Path Components (MPCs) that, given the description of a certain scenario, can physically propagate from the transmitter's to the receiver's location. These MPCs are characterized by angles of arrival and departure, power and delay, and can either be the direct component, or rays reflected from the scattering surfaces of

the environment [10]. Additionally, a RT, which is purely deterministic and only depends on the geometry of the scenario, can be combined with stochastic models for the generation of diffuse components to create a *Quasi-Deterministic (QD)* model. These depend on the roughness of the surface on which rays reflect, and are clustered around the main reflected component [15]. The modeling of these components is relevant at mmWaves as the wavelength approaches the scale of the surface roughness [9].

QD models for mmWaves have been introduced in [10], [15]. These papers, however, discuss the measurement process and the derivation of the parameters for the model, but only give a high-level overview of the mathematical formulation of the QD model. The goal of this paper is to fill that void, namely to provide the mmWave research community a detailed recipe on how to generate realizations of NIST's implementation of the IEEE 802.11ay QD model. We will discuss the generation of a channel instance step by step, precisely describing the parameters and random distributions, using an open source QD implementation developed by NIST and the University of Padova as a reference¹. Additionally, we will compare channels generated using this QD model with real measurements in an indoor environment at 60 GHz, to validate the accuracy of the model.

The rest of this paper is organized as follows. Section II introduces the notation that will be used throughout the paper. Section III reports the mathematical model, with the comparison in Section IV. Finally, Section V concludes the paper.

II. NOTATION

In the remainder of this paper, simple math font (e.g., a) is used for both scalar and vector variables, while bold math font is used for random variables (e.g., \mathbf{a}). The function $d(x_1, x_2)$ corresponds to the euclidean distance between points x_1 and x_2 in 3D space. The following notation and distributions for random variables are assumed:

- $\mathbf{X} \sim \mathcal{N}(\mu, \sigma^2)$: Normal distribution with $\mathbb{E}[\mathbf{X}] = \mu$ and $\text{var}(\mathbf{X}) = \sigma^2$
- $\mathbf{X} \sim \mathcal{R}(s, \sigma)$: Rician distribution where $s, \sigma \geq 0$. It can be generated as $\mathbf{X} = \sqrt{\mathbf{Y} + \mathbf{Z}}$, where $\mathbf{Y} \sim \mathcal{N}(s, \sigma^2)$, $\mathbf{Z} \sim \mathcal{N}(0, \sigma^2)$.
- $\mathbf{X} \sim \mathcal{L}(\mu, \sigma^2)$: Laplacian distribution with $\mathbb{E}[\mathbf{X}] = \mu$ and $\text{var}(\mathbf{X}) = \sigma^2$
- $\mathbf{X} \sim \mathcal{E}(\lambda)$: Exponential distribution with $\mathbb{E}[\mathbf{X}] = \frac{1}{\lambda}$ and $\text{var}(\mathbf{X}) = \frac{1}{\lambda^2}$
- $\mathbf{X} \sim \mathcal{U}[a, b]$: Uniform distribution in the closed interval $[a, b]$

III. MATHEMATICAL MODEL

In this section, we will provide a step-by-step tutorial on how to generate a channel with a QD model, with a precise and rigorous mathematical formulation.

¹Available at <https://github.com/signetlabdei/qd-realization/tree/feature/tretraversal>.

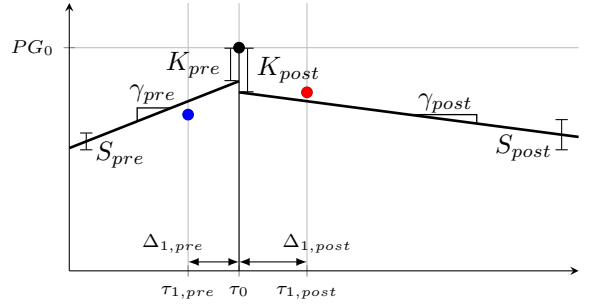


Figure 1: Graphical representation of QD parameters.

The QD model considers as a basis a deterministic channel, which can be computed through ray tracing for time t , given an environment geometry, and Transmitter (TX) and Receiver (RX) positions [14]. The computed Deterministic Rays (D-rays) will then be the baseline for the multipath components randomly generated by the QD model. If present, the direct ray is treated separately as it does not generate any diffuse component.

The QD model can be realized from the model for a first-order reflection and from it generalized to higher-order reflections. For reasons that will become clear later on, we define the instant in which the direct ray should arrive at the RX (even if it is actually blocked) as $t_0 = t + t_{\text{dir}}$, where $t_{\text{dir}} = \frac{d(\text{TX}, \text{RX})}{c}$, and c is the speed of light. From now on we will consider a frame of reference in the variable τ relative to time t_0 , where $\tau = 0$ corresponds to t_0 . Given this choice, the direct ray, if it exists, will arrive at time $\tau = 0$, whereas the reflected D-rays will arrive at times $\tau > 0$.

A. First-order reflections

Statistics for all rays are assumed independent of their arrival time. We thus consider, without loss of generality, a single reflected D-ray with arrival time $\tau_0 > 0$, path gain PG_0 , Angle of Departure (AoD) along the azimuth/elevation axes $AoD_{az/el,0}$, and Angle of Arrival (AoA) $AoA_{az/el,0}$. The same procedure will be repeated for all other reflected D-rays.

A cluster can be defined as the set with a D-ray and the corresponding MPCs. The total number of MPCs of a given cluster will be $N_{\text{MPC}} = N_{\text{pre}} + 1 + N_{\text{post}}$, including pre-cursors (i.e., diffuse components that are received before the D-ray), main cursor (i.e., the D-ray), and post-cursors (i.e., received after the D-ray). Based on some experimental evidence, we suggest to use $N_{\text{pre}} = 3$ and $N_{\text{post}} = 16$, although these numbers may vary in different locations and models.

The arrival times of the MPCs are modeled as a Poisson process, meaning that their inter-arrival times are independent and exponentially distributed. Namely, the post-cursors arrival times $\tau_{i,\text{post}}$ are random variables generated based on inter-arrival delays $\Delta_{i,\text{post}} = \tau_{i,\text{post}} - \tau_{i-1,\text{post}}$ as follows

$$\Delta_{i,\text{post}} | \tau_{i-1} \sim \mathcal{E}(\lambda_{\text{post}}), \quad (1)$$

for $i = 1, \dots, N_{\text{post}}$, where the arrival rate $\lambda_{\text{post}} \sim \mathcal{R}(s_{\lambda_{\text{post}}}, \sigma_{\lambda_{\text{post}}})$ is a random variable itself. With slight abuse

Algorithm 1 Single Reflection QD Generator

```

1: function GETMPCSFIRSTREFLECTION(Cursor:  $\tau_0$ ,  $PG_{0,D}$ ,
    $AoD_{az/el,0}$ ,  $AoA_{az/el,0}$ , Material)
2:    $RL \leftarrow \mathcal{R}(s_{RL,Material}, \sigma_{RL,Material})$ 
3:    $PG_0 = PG_{0,D} - (RL - \mu_{RL})$ 
4:   PreCursors  $\leftarrow$  COMPUTEPRE/POSTCURSORS( $\tau_0$ ,  $PG_0$ ,
    $AoD/AoA_{az/el,0}$ , Material)
5:   PostCursors  $\leftarrow$  COMPUTEPRE/POSTCURSORS( $\tau_0$ ,  $PG_0$ ,
    $AoD/AoA_{az/el,0}$ , Material)
   return PreCursors, Cursor, PostCursors

6: function COMPUTEPRE/POSTCURSORS( $\tau_0$ ,  $PG_0$ ,
    $AoD/AoA_{az/el,0}$ , Material)
7:    $\lambda \leftarrow \mathcal{R}(s_{\lambda,Material}, \sigma_{\lambda,Material})$ 
8:    $\Delta_i \leftarrow \mathcal{E}(\lambda)$ ,  $i = 1, \dots, N_{pre/post}$ 
9:    $\tau_i = \tau_0 \pm \sum_{j=1}^i \Delta_j$   $\triangleright$  Add for post-cursors, subtract for
   pre-cursors
10:  Remove pre-cursors with  $\tau_i < 0$ , update  $N_{pre/post}$ 
11:   $K_{dB} \leftarrow \mathcal{R}(s_{K,Material}, \sigma_{K,Material})$ 
12:   $\gamma \leftarrow \mathcal{R}(s_{\gamma,Material}, \sigma_{\gamma,Material})$ 
13:   $\sigma_{s,Material} \leftarrow \mathcal{R}(s_{\sigma_s,Material}, \sigma_{\sigma_s,Material})$ 
14:   $S_i \leftarrow \mathcal{N}(0, \sigma_{s,Material}^2)$ 
15:   $PG_i = PG_{0,D} - K_{dB} - 10 \log_{10}(e) \frac{|\tau_i - \tau_0|}{\gamma} +$ 
    $10 \log_{10}(e) S_i$ 
16:  Remove MPCs with  $PG_i \geq PG_0$ , update  $N_{pre/post}$ 
17:   $\sigma_\alpha \leftarrow \mathcal{R}(\mu_{\sigma_\alpha}, \sigma_{\sigma_\alpha})$ 
18:   $\alpha_{AoD/AoA_{az/el,i}} \leftarrow \mathcal{L}(0, \sigma_\alpha^2)$ 
19:   $AoD/AoA_{az/el,i} \leftarrow AoD/AoA_{az/el,0} + \alpha_{AoD/AoA_{az/el,i}}$ 
20:  Wrap angles in  $az = [0, 360)$ ,  $el = [0, 180]$ 
21:   $\phi_i \leftarrow \mathcal{U}[0, 2\pi)$ 
   return ( $\tau_i$ ,  $PG_i$ ,  $AoD/AoA_{az/el,i}$ )

```

of notation, we consider $\tau_{0,post} = \tau_0$, i.e., the time of arrival of the D-ray. Post-cursors arrival times are then computed as

$$\tau_{i,post} = \tau_{i-1,post} + \Delta_{i,post} = \tau_0 + \sum_{j=1}^i \Delta_{j,post}, \quad (2)$$

for $i = 1, \dots, N_{post}$. Please note that random parameters such as λ_{post} should be extracted independently for each D-ray.

Pre-cursors will be similarly generated, with the difference that Eq. (2) will subtract inter-arrival delay, thus making $\tau_{i,pre} < \tau_0$ for $i = 1, \dots, N_{pre}$.

Since the number of pre/post-cursors was empirically extrapolated from measured data from [10], during the QD model generation some of them may not follow some basic assumptions. For example, when a D-ray has a delay τ_0 close to 0, some of its generated pre-cursors might arrive before the direct ray itself. Since this situation cannot happen in the physical reality, rays with $\tau_{i,pre} < 0$ are removed and N_{pre} is consequently updated.

The path gain of the D-ray is

$$PG_0 = 20 \log_{10} \left(\frac{\lambda_c}{4\pi \ell_{ray}} \right) - \mathbf{RL}_{dB}, \quad (3)$$

where λ_c is the wavelength of the carrier frequency, ℓ_{ray} is the total ray length, and $\mathbf{RL} \sim \mathcal{R}(s_{RL}, \sigma_{RL})$ is the random reflection loss factor given by the reflecting surface's material.

If only the deterministic part of the ray-tracer is considered, the path gain $PG_{0,D}$ only includes the mean reflection loss μ_{RL} .

Once the arrival times τ_i are known, the path gains for the MPCs can be computed as

$$PG_{pre/post,i,dB} = PG_{0,dB} - K_{pre/post,dB} + \frac{|\tau_{i,pre/post} - \tau_0|}{\gamma_{pre/post}} (10 \log_{10} e) + (10 \log_{10} e) S_{pre/post}, \quad (4)$$

where

- $K_{pre/post,dB} \sim \mathcal{R}(s_{K_{pre/post}}, \sigma_{K_{pre/post}})$ is a loss factor,
- $\gamma_{pre/post} \sim \mathcal{R}(s_{\gamma_{pre/post}}, \sigma_{\gamma_{pre/post}})$ is the power-delay decay constant,
- $S_{pre/post} \sim \mathcal{N}(0, \sigma_{s,pre/post}^2)$ is the power-delay decay standard deviation, where $\sigma_{s,pre/post} \sim \mathcal{R}(s_{\sigma_{s,pre/post}}, \sigma_{\sigma_{s,pre/post}})$.

While $K_{pre/post,dB}$, $\gamma_{pre/post}$, and $\sigma_{s,pre/post}$ are independent across clusters, and $S_{pre/post}$ is independently extracted for each MPC.

Since the main cursor is that with the maximum PG when extracting the statistics from the measurements, MPCs with $PG_{pre/post,i} \geq PG_{0,D}$ are removed, updating, in this case, $N_{pre/post}$.

Finally, the angle of departure in azimuth (and similarly the AoD in elevation and the AoAs in azimuth and elevation) of the MPCs are computed as

$$AoD_{az,i} = AoD_{az,0} + \alpha_{AoD,az,i}, \quad (5)$$

where $\alpha_{AoD,az,i} \sim \mathcal{L}(0, \sigma_{\alpha_{AoD,az}}^2)$ is the angle spread. The variance $\sigma_{\alpha_{AoD,az}}^2 \sim \mathcal{R}(s_{\sigma_{\alpha_{AoD,az}}^2}, \sigma_{\sigma_{\alpha_{AoD,az}}^2})$ is itself a random variable independently extracted for each cluster.

Finally, the phase shift ϕ_i due to both diffusion and Doppler shift is considered $\mathcal{U}[0, 2\pi)$ independently for each diffuse MPC.

B. Higher-order reflections

For the n^{th} reflection order, with $n > 1$, multiple heuristics can be thought of to compute the diffuse components. Unfortunately, the measurements taken and the models adopted to process them do not allow for a reliable confirmation of the proposed heuristics, but an extension to higher reflection orders is nevertheless needed for inclusion in a generic ray-tracer.

The path gain for specular rays with n reflections is extended as follows:

$$PG_0 = 20 \log_{10} \left(\frac{\lambda_c}{4\pi \ell_{ray}} \right) - \sum_{i=1}^n \mathbf{RL}_{i,dB}, \quad (6)$$

where $\mathbf{RL}_{i,dB} \sim \mathcal{R}(s_{RL,i}, \sigma_{RL,i})$, and $(s_{RL,i}, \sigma_{RL,i})$ refers to the statistics associated to the material of the i -th reflector of the given ray.

We propose two simple heuristics: a complete multiple reflection QD model and a reduced multiple reflection QD model.

Algorithm 2 Reduced Multiple Reflection QD Generator

```

1: function GETMPCSMULTIPLEREFLECTION(Cursor, Material-
   List, MaterialLibrary)
2:   CursorOutput  $\leftarrow$  Cursor
3:   for Material  $\in$  MaterialList do
4:     OtherMaterialsList  $\leftarrow$  MaterialList  $\setminus$  {Material}
5:     PreCursors, PostCursors  $\leftarrow$   $\emptyset$ 
6:     CurrentPreCursors, CursorOutput, CurrentPostCursors  $\leftarrow$ 
       GETMPCSFIRSTREFLECTION(CursorOutput, Material)
7:     PreCursors  $\leftarrow$  Concatenate(PreCursors, OTHERMATERI-
       ALSREFLLOSS(CurrentPreCursors, OtherMaterialsList, Materi-
       alLibrary))
8:     PostCursors  $\leftarrow$  Concatenate(PostCursors, OTHERMATE-
       RIALSREFLLOSS(CurrentPostCursors, OtherMaterialsList, Materi-
       alLibrary))
   return PreCursors, CursorOutput, PostCursors

9: function OTHERMATERIALSREFLLOSS(Cursors, OtherMateri-
   alsList, MaterialLibrary)
10:  for Cursor  $\in$  Cursors do
11:    for Material  $\in$  OtherMaterialsList do
12:       $RL \leftarrow \mathcal{R}(s_{RL,Material}, \sigma_{RL,Material})$ 
13:      Cursor.PG  $\leftarrow$  Cursor.PG + ( $RL - \mu_{RL,Material}$ )
   return Cursors
  
```

Complete multiple reflection QD model: Upon the first scattering event, all components produced – both specular and diffuse – behave as independent components and their remaining paths are traced accordingly. We assume that every diffuse ray closely follows the path of the main cursor and further generates $N_{pre} + N_{post}$ diffuse MPCs at each bounce. The total number of MPCs generated by a single deterministic rays at the n -th reflection will thus be $N_{MPC} \sim (N_{pre} + 1 + N_{post})^n$.

Reduced multiple reflection QD model: In order to reduce the exponential complexity of the complete model, the reduced model neglects diffuse rays beyond a first order given their multiplicatively high attenuation. Instead, only diffuse rays generated directly by the deterministic ray are taken into account, each generated with the QD parameters relative to the impinging reflecting surface. Moreover, we assume that every diffuse component closely follows the main cursor, thus reflecting on the same reflectors (see Algorithm 2). Consequently, every reflector produces $N_{pre} + N_{post}$ diffuse components, thus yielding a maximum of $N_{MPC} \sim n(N_{pre} + N_{post}) + 1$, including the deterministic ray and possible rays discarded during their generation (see Section III-A).

IV. COMPARISON WITH MEASUREMENTS

Given the structure of this QD model, every material must have a set of parameters for it to be appropriately simulated. It follows that given the CAD file of an environment, every surface must be associated with a material with all the necessary simulation parameters taken, for example, from a material library.

We report in the following tables examples of material libraries from NIST’s Lecture Room, reformulating the mean

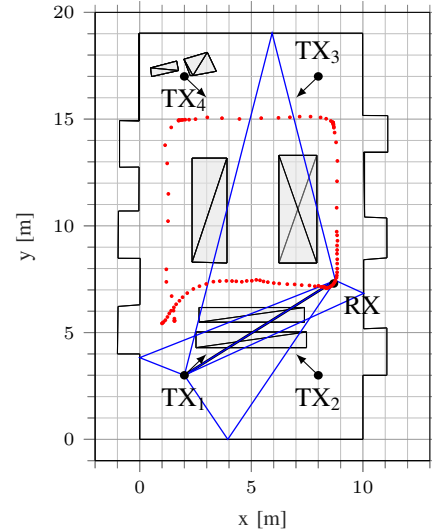


Figure 2: CAD model of NIST’s lecture room. The 108 RX positions from the measurement traces are shown in red. As an example, the direct and first reflection rays generated with the RT for TX₁ and the specific RX position are shown in black and blue, respectively.

and variance provided per material [10] into the s and σ parameters needed to generate the random parameters of the model. Measured data were taken from different TX positions pointing towards the center of the room, where a mobile RX sounder moved around the tables. Specifically, as shown in Fig. 2, considering the bottom-left corner as the origin $(x_0, y_0, z_0) = (0, 0, 0)$, TX₁ is positioned in (2, 3, 2.5) m, TX₂ in (8, 3, 2.5) m, TX₃ in (8, 17, 2.5) m, TX₄ in (2, 17, 2.5) m, and the RX performs a loop around the table.

Given that the channel sounder’s TX had a limited angular Field-of-View (FoV), it was possible to characterize different surfaces, e.g., different walls by varying the TX positions during the measurement campaign. The model parameters per position have been reformatted accordingly in Table I. Please note that, given the geometry of the room and the limited FoV, it was not possible to properly characterize some materials, such as the floor [10]. For these materials, since no characterization was available, the pre/post cursors were not generated and the statistics for the reflection loss were taken from the ceiling instead.

Fig. 3 shows an example of measured channel compared to the deterministic ray-traced channel for the scenario of Fig. 2. As can be seen, the direct ray is correctly identified both in the power-delay domain and in the angles domains, while other rays only partially resemble the measurements. This is due to (i) the approximated CAD model which may be missing some relevant reflectors and (ii) inaccuracies in the measurements.

While delays shown in Fig. 3a are in good accord between measurements and RT simulation, path gains are less precise, due to the random reflection losses experienced by the rays. Notice also that the TX only has antennas towards the front (as shown by the antenna pattern in Fig. 3b), thus, rays predicted by the RT to depart with an azimuth angle between 135° and 315° were not part of the real measurements. Most of all, though, it is easily noticeable that there exist clusters of rays

Table I: NIST's Lecture Room material library.

		Left Wall (TX ₂)	Bottom Wall (TX ₃)	Right Wall (TX ₁)	Top Wall (TX ₁)	Tables (TX ₁)	Ceiling (TX ₁)
$K_{dB} \sim \mathcal{R}(s, \sigma)$	$(s_{K_{pre}}, \sigma_{K_{pre}})$ $(s_{K_{post}}, \sigma_{K_{post}})$	(5.1196, 1.7485) (6.2208, 3.5421)	(1.4809, 2.1325) (7.1809, 2.5325)	(0, 0) (0.2641, 3.1699)	(0.5913, 4.5206) (0.33, 3.7213)	(0, 0) (3.7738, 1.8748)	(3.6167, 7.2715) (7.1103, 2.2712)
$\gamma \sim \mathcal{R}(s, \sigma)$	$(s_{\gamma_{pre}}, \sigma_{\gamma_{pre}})$ $(s_{\gamma_{post}}, \sigma_{\gamma_{post}})$	(0.6742, 0.9992) (0.0658, 1.2034)	(0.9006, 0.2325) (0.6881, 0.3566)	(0, 0) (0.0412, 0.8648)	(0.0094, 0.2285) (0.0792, 1.1572)	(0, 0) (0.53, 0.4837)	(0.9595, 0.901) (0.0717, 1.2794)
$\sigma_s \sim \mathcal{R}(s, \sigma)$	$(s_{\sigma_s, pre}, \sigma_{\sigma_s, pre})$ $(s_{\sigma_s, post}, \sigma_{\sigma_s, post})$	(0.0119, 0.3087) (0.4144, 0.1507)	(0.5553, 0.129) (0.26, 0.1003)	(0, 0) (0.6367, 0.3209)	(0.243, 0.273) (0.201, 0.1901)	(0, 0) (0.3309, 0.4614)	(0.2122, 0.0935) (0.7679, 0.2484)
$\lambda \sim \mathcal{R}(s, \sigma)$	$(s_{\lambda_{pre}}, \sigma_{\lambda_{pre}})$ $(s_{\lambda_{post}}, \sigma_{\lambda_{post}})$	(0.9775, 0.3449) (0.8153, 0.6948)	(0.9172, 0.2241) (1.4106, 0.5832)	(0, 0) (0.9879, 0.4235)	(0.619, 1.1299) (0.8655, 0.3762)	(0, 0) (0.8099, 0.076)	(0.8119, 0.2421) (0.7785, 0.1426)
$\sigma_\alpha \sim \mathcal{R}(s, \sigma)$	$(s_{\sigma_\alpha, az}, \sigma_{\sigma_\alpha, az})$ $(s_{\sigma_\alpha, el}, \sigma_{\sigma_\alpha, el})$	(0.1016, 2.2504) (2.9947, 1.6613)	(1.9426, 1.5726) (2.6946, 1.3948)	(3.2889, 1.3202) (3.2812, 1.8865)	(2.117, 2.1206) (2.741, 1.7964)	(1.6594, 3.1974) (4.0345, 2.6859)	(1.9829, 0.9094) (2.696, 1.1135)
$RL \sim \mathcal{R}(s, \sigma)$	(s_{RL}, σ_{RL}) μ_{RL}	(9.8412, 3.4424) 10.7	(8.5025, 4.2343) 9.84	(10.1562, 3.5164) 10.8	(6.7238, 5.9352) 9.27	(5.2106, 3.4013) 6.58	(6.5833, 2.1943) 6.9

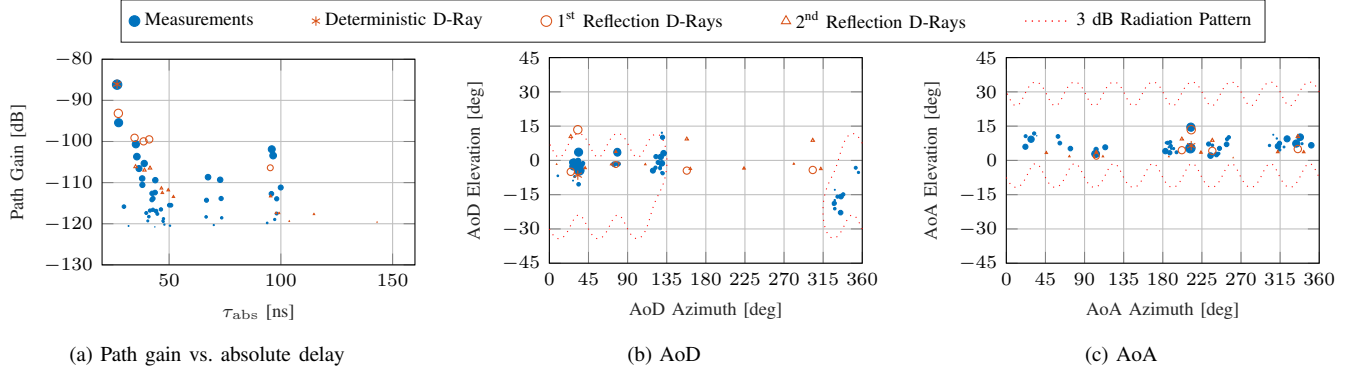


Figure 3: Example of comparison between measurements and ray-tracer, based on the channel between TX₁ and the RX shown in Fig. 2 in the bottom left corner of the loop. In (a), τ_{abs} represents the absolute delay of each ray. (b) and (c) show the 3 dB radiation patterns of the channel sounders described in [10] approximated with Gaussian beams. In fact, MPCs outside of these regions are not detected in the measurements.

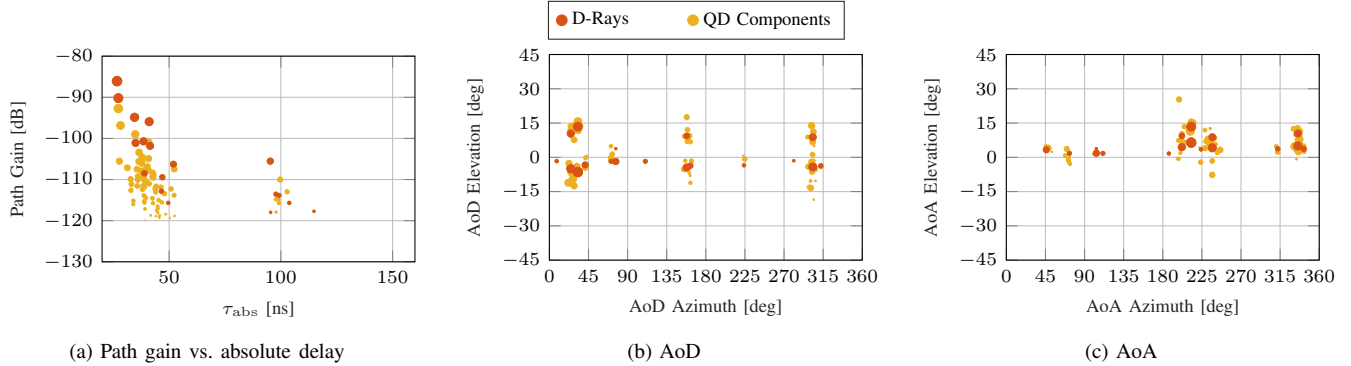


Figure 4: Reduced multiple reflection QD model applied to RT-based channel traces with up to 2nd order reflections. Rays with path gain below -120 dB are not shown, to more closely resemble the dynamic range of the channel sounder.

well defined in the joined path gain, delay, AoD, AoA domain, and are missing, instead in the channel generated by the RT. Such clusters do not arise from higher order reflections (not shown here), but rather from diffuse MPCs, thus highlighting the need for a valid diffuse QD model.

Figs. 4 and 5 show how the proposed QD model enhances the realism of a purely deterministic channel, making it significantly more similar to the measured one. Specifically, Fig. 4 reports an example of a specific channel instance, based on the CAD model shown in Fig. 2 and for the same TX/RX locations of Fig. 3. With respect to the RT specular reflections from Fig. 3, the deterministic rays (in orange), which are

generated up to second order reflections, also include a random reflection loss component in the path gain. The diffuse rays added to the model are plotted in blue, with sizes proportional to the respective path gain. By comparing Fig. 4 with Fig. 3, it is clear that the D-rays alone are not able to fully model the complexity of a real channel, and that the proposed QD model can instead play an important role to this regard. In fact, empirically, rays are parts of clusters with small variations in the angular and delay domains, and large variations in the power gain domain.

Furthermore, the effects of the added rays are clearly shown in Fig. 5, which plots the Cumulative Distribution Functions

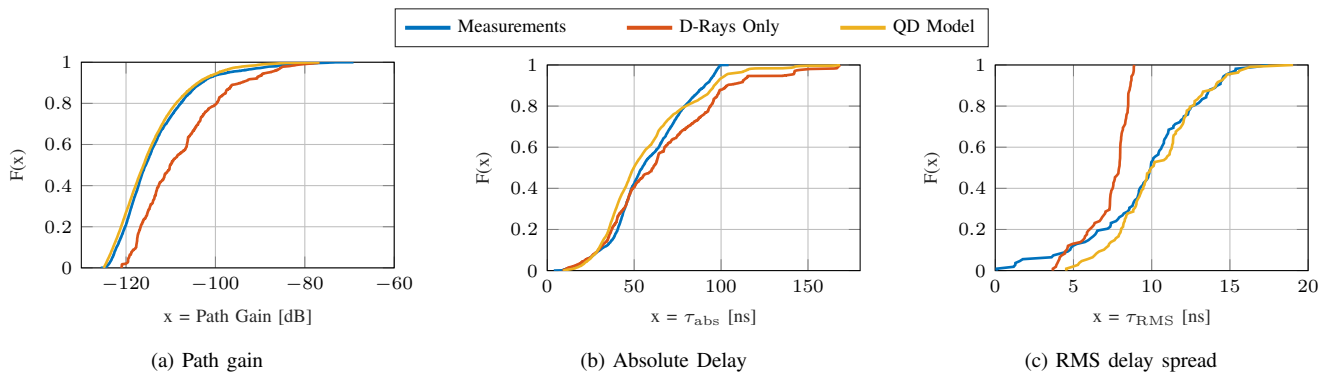


Figure 5: Comparison between CDFs of MPC path gain, absolute delay, and RMS delay spread with and without QD model with respect to the measurements.

(CDFs) of the path gain (Fig. 5a), the absolute delay (Fig. 5b), and the RMS delay spread (Fig. 5c), similar to the RMS angle spread shown in [10], for the multipath components of the scenarios. The CDFs show the combined statistics of the mmWave channel between TX₁ and 108 RX positions shown in red in Fig. 2). Notably, it is clear how the delays and path gains generated with the proposed QD model are significantly closer to the real measurements with respect to purely deterministic rays alone, with CDF fit improvements from 73 % to 86 % (i.e., Kolmogorov-Smirnov (KS) test improvements of 0.13) for the path gain, from 86 % to 89 % (i.e., KS test improvements of 0.03) for the absolute delay, and from 33 % to 87 % (i.e., KS test improvements of 0.54) for the RMS delay spread.

V. CONCLUSIONS

Performance evaluation is a fundamental part of the design of 5G mmWave networks. To that end, an accurate channel model allows researchers to generate reliable simulation results, that can qualitatively and quantitatively describe what can be expected when using real devices. In this paper, we introduce a mathematical formulation for a class of mmWave channels, i.e., the QD models, that can closely simulate the propagation of rays in a specific environment. We provided a step-by-step tutorial on how such models can be implemented, including the parameters and random distributions obtained from a NIST measurement campaign [10]. We then compared the results that can be obtained with an open source implementation of the model with the real measurement traces, showing improvements in the KS test for path gain (0.131), delay (0.03), and RMS delay spread (0.537).

As future work, we will further extend the QD model with material libraries from other measurement campaigns, and study methods to reduce the computational complexity involved in the ray and channel matrices generation, as in [16].

REFERENCES

- [1] T. Bai and R. W. Heath, "Coverage and rate analysis for millimeter-wave cellular networks," *IEEE Transactions on Wireless Communications*, vol. 14, no. 2, pp. 1100–1114, Feb. 2015.
- [2] M. Mezzavilla, M. Zhang, M. Polese, R. Ford, S. Dutta, S. Rangan, and M. Zorzi, "End-to-End Simulation of 5G mmWave Networks," *IEEE Communications Surveys & Tutorials*, vol. 20, no. 3, pp. 2237–2263, Third Quarter 2018.
- [3] H. Assasa, J. Widmer, J. Wang, T. Ropitault, and N. Golmie, "An Implementation Proposal for IEEE 802.11ay SU/MU-MIMO Communication in ns-3," in *Proceedings of the 2019 Workshop on Next-Generation Wireless with ns-3*, Jun. 2019, pp. 26–29.
- [4] N. Patriciello, S. Lagen, B. Bojovic, and L. Giupponi, "An E2E Simulator for 5G NR Networks," *Simulation Modelling Practice and Theory*, vol. 96, Nov. 2019.
- [5] M. Polese and M. Zorzi, "Impact of Channel Models on the End-to-End Performance of mmWave Cellular Networks," in *IEEE 19th International Workshop on Signal Processing Advances in Wireless Communications (SPAWC)*, Jun. 2018.
- [6] S. Rangan, T. S. Rappaport, and E. Erkip, "Millimeter-Wave Cellular Wireless Networks: Potentials and Challenges," *Proceedings of the IEEE*, vol. 102, no. 3, pp. 366–385, Mar. 2014.
- [7] T. S. Rappaport, S. Sun, R. Mayzus, H. Zhao, Y. Azar, K. Wang, G. N. Wong, J. K. Schulz, M. Samimi, and F. Gutierrez, "Millimeter wave mobile communications for 5G cellular: It will work!" *IEEE Access*, vol. 1, pp. 335–349, 2013.
- [8] S. Hur, S. Baek, B. Kim, Y. Chang, A. F. Molisch, T. S. Rappaport, K. Haneda, and J. Park, "Proposal on Millimeter-Wave Channel Modeling for 5G Cellular System," *IEEE Journal of Selected Topics in Signal Processing*, vol. 10, no. 3, pp. 454–469, Apr. 2016.
- [9] C. Gentile, P. B. Papazian, R. Sun, J. Senic, and J. Wang, "Quasi-Deterministic Channel Model Parameters for a Data Center at 60 GHz," *IEEE Antennas and Wireless Propagation Letters*, vol. 17, no. 5, pp. 808–812, May 2018.
- [10] C. Lai, R. Sun, C. Gentile, P. B. Papazian, J. Wang, and J. Senic, "Methodology for multipath-component tracking in millimeter-wave channel modeling," *IEEE Transactions on Antennas and Propagation*, vol. 67, no. 3, pp. 1826–1836, Mar. 2019.
- [11] I. A. Hemadeh, K. Satyanarayana, M. El-Hajjar, and L. Hanzo, "Millimeter-Wave Communications: Physical Channel Models, Design Considerations, Antenna Constructions, and Link-Budget," *IEEE Communications Surveys and Tutorials*, vol. 20, no. 2, pp. 870–913, Second Quarter 2018.
- [12] T. S. Rappaport, Y. Xing, G. R. MacCartney, A. F. Molisch, E. Mellios, and J. Zhang, "Overview of Millimeter Wave Communications for Fifth-Generation (5G) Wireless Networks – With a Focus on Propagation Models," *IEEE Trans. Antennas Propag.*, vol. 65, no. 12, pp. 6213–6230, Dec. 2017.
- [13] 3GPP, "Study on channel model for frequencies from 0.5 to 100 GHz," 3rd Generation Partnership Project (3GPP), Technical Report (TR) 38.901, Jun. 2018, version 15.0.0.
- [14] V. Degli Esposti, F. Fuschini, E. M. Vitucci, M. Barbiroli, M. Zoli, L. Tian, X. Yin, D. A. Dupleich, R. Müller, C. Schneider, and R. S. Thomä, "Ray-Tracing-Based mm-Wave Beamforming Assessment," *IEEE Access*, vol. 2, pp. 1314–1325, Dec. 2014.
- [15] A. Maltsev, A. Pudeyev, A. Lomayev, and I. Bolotin, "Channel modeling in the next generation mmWave Wi-Fi: IEEE 802.11ay standard," in *22th European Wireless Conference*, May 2016.
- [16] M. Lecci, P. Testolina, M. Giordani, M. Polese, T. Ropitault, C. Gentile, N. Varshney, A. Bodi, and M. Zorzi, "Simplified ray tracing for the millimeter wave channel: A performance evaluation," in *Proceedings of the Workshop on Information Theory and Applications (ITA)*, Feb. 2020.